3556 *Chem. Mater.* **2010,** *22,* 3556–3567
DOI:10.1021/cm100871g

CHEMISTRY OF MATERIALS
Article

# Pathway from a Molecular Precursor to Silver Nanoparticles: The Prominent Role of Aggregative Growth

Vernal N. Richards,[†] Nigam P. Rath,[‡] and William E. Buhro*[,†]

[†]*Department of Chemistry and Center for Materials Innovation, Washington University, St. Louis, Missouri 63130-4899, and* [‡]*Department of Chemistry and Biochemistry and Center for Nanoscience, University of Missouri−St. Louis, St. Louis, Missouri 63121*

*Received March 26, 2010. Revised Manuscript Received May 4, 2010*

A mechanistic study of Ag-nanoparticle growth by reaction of $[(PPh_3)_2Ag(O_2CC_{13}H_{27})]$ and AIBN is reported. The half-life for precursor disappearance at 130.0 ± 0.1 °C under the reaction conditions is determined to be 3.65 ± 0.42 min, which defines the time scale for classical (LaMer) nucleation and growth to be within the first 15 min (4 half-lives). The nanoparticle-growth kinetics are separately determined by TEM monitoring and UV−visible spectroscopy. Fits to the kinetic data establish that the active-growth regime extends to 58 min, and that Ostwald ripening ensues shortly thereafter. Evidence for an aggregative nucleation and growth process is obtained. The quantitative data indicate that classical nucleation and growth, aggregative nucleation and growth, and Ostwald ripening occur in consecutive time regimes with little overlap, and that nanoparticle growth is dominated by the aggregative regime. Aggregative growth should be considered a potential contributing mechanism in all nanoparticle-forming reactions.

## Introduction

In this study, we have elucidated the entire pathway for the growth of Ag nanoparticles from the myristate precursor $[(PPh_3)_2Ag(O_2CC_{13}H_{27})]$. We have separately determined the kinetics of precursor disappearance and nanoparticle growth. We have directly observed a second, aggregative nucleation process. The combined results demonstrate that the growth of Ag nanoparticles under the conditions employed is dominated by aggregative processes. Finally, we argue that aggregative nucleation and growth is a more-significant component of nanoparticle formation than is generally recognized.

The two commonly invoked mechanisms for nanoparticle growth are classical nucleation and growth (the LaMer mechanism),[1−6] and Ostwald ripening.[7,8] In the LaMer or classical mechanism,[9−11] growth is initiated from crystal nuclei, and continued by molecular addition to the surfaces of the supercritical crystal seeds. Ostwald ripening requires a nanoparticle size distribution, in which the smaller nanoparticles dissolve to supply nutrient for the growth of the larger nanoparticles.[12]

In the less-considered aggregative mechanism,[13−16] small primary nanocrystals aggregate and coalesce to form viable nanoparticles capable of further growth by aggregation and coalescence with additional primary nanocrystals (Scheme 1).[17−21] Aggregative growth may proceed by a second nucleation process, in which the growth-viable nanoparticles are assembled from primary nanocrystals.[21]

Nanoparticles prepared from molecular precursors are generally presumed to have grown by the classical LaMer mechanism.[1−5] Nanoparticles prepared from smaller nanoparticles are generally presumed to have grown by Ostwald ripening.[7,8] However, we previously showed that small, primary Au nanocrystals coarsened by an aggregative nucleation-and-growth pathway.[21] Here we show that Ag nanoparticles grown from a molecular precursor

*To whom correspondence should be addressed. E-mail: buhro@wustl.edu.

(1) Morales, M. P.; González-Carreño, T.; Serna, C. J. *J. Mater. Res.* **1992**, *7*, 2538–2545.
(2) Murray, C. B.; Norris, D. J.; Bawendi, M. G. *J. Am. Chem. Soc.* **1993**, *115*, 8706–8715.
(3) Saunders, A. E.; Sigman, M. B.; Korgel, B. A. *J. Phys. Chem. B* **2004**, *108*, 193–199.
(4) Drofenik, M.; Kristl, M.; Žnidaršič, A.; Hanžel, D.; Lisjak, D. *J. Am. Ceram. Soc.* **2007**, *90*, 2057–2061.
(5) Robb, D. T.; Privman, V. *Langmuir* **2008**, *24*, 26–35.
(6) Zheng, H.; Smith, R. K.; Jun, Y.-w.; Kisielowski, C.; Dahmen, U.; Alivisatos, A. P. *Science* **2009**, *324*, 1309–1312.
(7) Luo, G. *Mater. Lett.* **2007**, *61*, 1039–1041.
(8) Meli, L.; Green, P. F. *ACS Nano* **2008**, *2*, 1305–1312.
(9) LaMer, V. K.; Dinegar, R. H. *J. Am. Chem. Soc.* **1950**, *72*, 4847–4854.
(10) LaMer, V. K. *Ind. Eng. Chem.* **1952**, *44*, 1270–1277.
(11) Reiss, H. *J. Chem. Phys.* **1951**, *19*, 482–487.
(12) Voorhees, P. W. *J. Stat. Phys.* **1985**, *38*, 231.
(13) Finney, E. E.; Finke, R. G. *Chem. Mater.* **2008**, *20*, 1956–1970.
(14) Van Hyning, D. L.; Klemperer, W. G.; Zukoski, C. F. *Langmuir* **2001**, *17*, 3128–3135.
(15) Penn, R. L.; Banfield, J. F. *Science* **1998**, *281*, 969–971.
(16) Uyeda, N.; Nishino, M.; Suito, E. *J. Colloid Interface Sci.* **1973**, *43*, 264–275.
(17) Matijević, E.; Goia, D. *Croatica Chem. Acta* **2007**, *80*, 485–491.
(18) Privman, V.; Goia, D. V.; Park, J.; Matijević, E. *J. Colloid Interface Sci.* **1999**, *213*, 36–45.
(19) Libert, S.; Gorshkov, V.; Goia, D.; Matijević, E.; Privman, V. *Langmuir* **2003**, *19*, 10679–10683.
(20) Privman, V. *Ann. N.Y. Acad. Sci.* **2009**, *1161*, 508–525.
(21) Shields, S. P.; Richards, V. N.; Buhro, W. E. *Chem. Mater.* **2010**, DOI:10.1021/cm100458b.

 Published on Web 05/13/2010 

**Scheme 1. Schematic Depiction of Three Stages of Nanocrystal Growth—Aggregative Nucleation, Aggregative Growth, and Ostwald Ripening—and Commonly Observed Sigmoidal Kinetic Profile[a]**

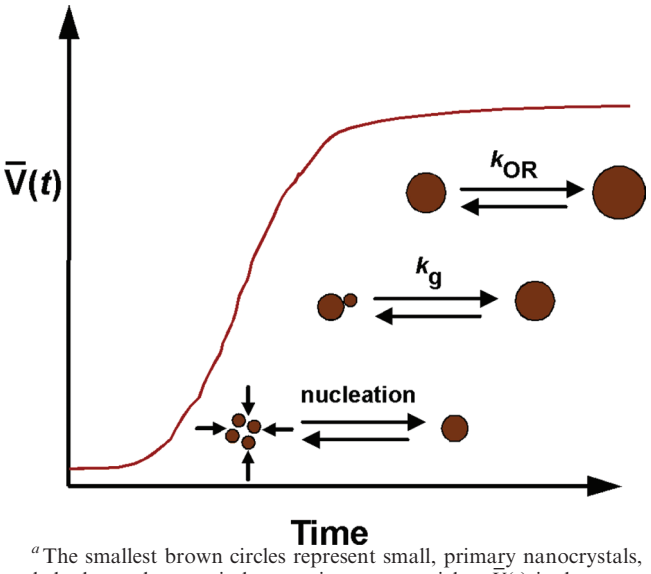


[a] The smallest brown circles represent small, primary nanocrystals, and the larger brown circles growing nanoparticles. $\bar{V}(t)$ is the mean nanocrystal volume at time $t$.

also form by an aggregative nucleation-and-growth mechanism.

As detailed herein, the primary evidence against classical nucleation and growth as the dominant mechanism is a comparison of the rates of precursor disappearance and nanoparticle growth. We show quantitatively that the $[(PPh_3)_2Ag(O_2CC_{13}H_{27})]$ precursor is substantially consumed near the onset of the active growth of Ag nanoparticles. The different time scales of the two processes preclude a classical mechanism as the major component of the growth pathway.[14] Furthermore, the observation of a second nucleation event involving small, primary Ag nanocrystallites is inconsistent with classical nucleation and growth.[17−21]

Ostwald ripening is excluded as the predominant growth mechanism by the observation of pseudosigmoidal nanoparticle growth kinetics,[13,21−25] bimodal nanoparticle size distributions at early times,[17−21,26−28] and mature nanoparticles that are essentially all polycrystals.[15,16,29−32] Additionally, we show that Ostwald ripening does occur, but only after the active-growth period. Finally, the second, aggregative nucleation process is also inconsistent with Ostwald ripening, which is not a nucleation-driven process.[12]

Many of the arguments and mechanistic analyses employed here to establish aggregative nucleation and growth were developed in our prior study of Au nanoparticle coarsening. We show here that an aggregative mechanism may also dominate nanoparticle-growth processes that are initiated from molecular precursors. Therefore, aggregative nucleation and growth should be considered as a potential contributing mechanism in all nanoparticle-growth procedures.

## Experimental Section

**General Methods and Materials.** Poly(1-hexadecene)$_{0.67}$-*co*-(1-vinylpyrrolidone)$_{0.33}$, myristic acid (99%), silver nitrate (99%), benzene (99%), 1,2-dichlorobenzene (99%), and cyclohexane (99%) were purchased from Aldrich and used as received. Azoisobutyronitrile (AIBN) was purchased from Aldrich and purified by recrystallization from hot ethanol. All reactions were conducted in the ambient atmosphere. Mass spectrometry was performed using a Bruker Maxis Q-TOF mass spectrometer. $^{31}$P NMR spectra were collected on a Varian INOVA-300 spectrometer at 121 MHz, and $^{13}C\{^1H\}$NMR spectra on a Varian INOVA-600 spectrometer at 150 MHz. TEM images were recorded using a JEOL 2000FX microscope operating at 200 kV. High-resolution TEM (HRTEM) images were recorded on a JEOL JEM-2100F microscope operating at 200 kV. UV−visible spectra were recorded on a Varian Carey 1E spectrophotometer at room temperature. Elemental analyses were performed by Galbraith Laboratories.

**Synthesis of Silver Myristate ($C_{13}H_{27}CO_2Ag$).** Myristic acid (9.83 g, 43.0 mmol) was dissolved in acetone (250 mL) in a 500 mL Erlenmeyer flask. To the stirring myristic acid solution, silver nitrate (7.31 g, 43.0 mmol) dissolved in 3:1 v/v water/acetone mixture (200 mL) was added, resulting in immediate precipitation. The suspension was filtered and the precipitate washed with water (ca. 200 mL), followed by acetone (ca. 100 mL). The solid was dried in vacuo at 100 °C for 72 h. Yield: 8.54 g, 25.5 mmol, 85%.

Anal. Calcd for $C_{13}H_{27}CO_2Ag$: C, 50.15; H, 8.11. Found, C, 49.52; H, 8.10; N, < 0.5. All values are given as percentages.

**Synthesis of Bis(triphenylphosphine)silver(I) Myristate [$(PPh_3)_2Ag(O_2CC_{13}H_{27})$].** Silver myristate (6.0 g, 18 mmol) was added to benzene (200 mL) containing dissolved triphenylphosphine (11.0 g, 42.0 mmol) in a 500 mL round-bottom flask. The stirred mixture was refluxed for one hour, resulting in the dissolution of the silver myristate. While it was still warm, the solution was transferred to a 500 mL beaker, covered, and left to cool. After the beaker was allowed to stand (24 h), colorless spindle-like crystals appeared. The crystals were separated from the supernatant by filtration, washed with acetone (25 mL), and dried in vacuo. Yield: 11.28 g, 13.12 mmol, 73%; mp 111−113 °C.

Anal. Calcd for $[(PPh_3)_2Ag(O_2CC_{13}H_{27})]$: C, 69.85; H, 6.88; P, 7.20. Found, C, 69.76; H, 6.45; P, 7.37; N, <0.5. All values are given as percentages. $^1$H NMR (300 MHz, $d_6$-acetone, $\delta$): 7.3−7.5 (m, 30 H, $C_6H_5$), 2.1 (t, 2H, $CH_2$), 1.5 (m, 2H, $CH_2$), 1.3 (m, 20H, $CH_2$), 0.9 (t, 3H, $CH_3$). $^{31}P\{^1H\}$ NMR (121 MHz, $d_6$-acetone, −80 °C, ppm): 8.64 (d, $^1J$(P,$^{109}$Ag) = 471.98 Hz), 8.63 ($^1J$(P,$^{107}$Ag) = 414.13 Hz). $^{31}P\{^1H\}$ NMR (121 MHz, $d_6$-acetone, 25 °C, ppm): 8.7 (s).

**Collection of Kinetic Data for Silver Nanoparticle Growth.** In a typical trial, bis(triphenylphosphine)silver(I) myristate (0.044 g,

(22) Hornstein, B. J.; Finke, R. G. *Chem. Mater.* **2004**, *16*, 139–150.
(23) Besson, C.; Finney, E. E.; Finke, R. G. *J. Am. Chem. Soc.* **2005**, *127*, 8179–8184.
(24) Besson, C.; Finney, E. E.; Finke, R. G. *Chem. Mater.* **2005**, *17*, 4925–4938.
(25) Ott, L. S.; Finke, R. G. *Chem. Mater.* **2008**, *20*, 2592–2601.
(26) Drews, T. O.; Katsoulakis, M. A.; Tsapatsis, M. *J. Phys. Chem. B* **2005**, *109*, 23879–23887.
(27) Drews, T. O.; Tsapatsis, M. *Microporous Mesoporous Mater.* **2007**, *101*, 97–107.
(28) Bogush, G. H.; Zukoski, C. F. *J. Colloid Interface Sci.* **1991**, *142*, 19–34.
(29) Bisson, L.; Boissiere, C.; Nicole, L.; Grosso, D.; Jolivet, J. P.; Thomazeau, C.; Uzio, D.; Berhault, G.; Sanchez, C. *Chem. Mater.* **2009**, *21*, 2668–2678.
(30) Huang, F.; Zhang, H.; Banfield, J. F. *Nano Lett.* **2003**, *3*, 373–378.
(31) Turkevich, J. *Gold Bull.* **1985**, *18*, 86–91.
(32) Chen, M.; Feng, Y.; Wang, X.; Li, T.; Zhang, J.; Qian, D. *Langmuir* **2007**, *23*, 5296–5304.

0.051 mmol) and AIBN (0.05 g, 0.3 mmol) were dissolved in 4% w/w poly(1-hexadecene)$_{0.67}$-*co*-(1-vinylpyrrolidone)$_{0.33}$ in 1,2-dichlorobenzene (10 mL) in a 50 mL round-bottom flask under ambient air. The stirred mixture was heated at 130.0 ± 0.1 °C in a 300 mL oil bath connected to an Ace Glass temperature controller. Aliquots were taken at specific time intervals by removing approximately 0.5 mL of the solution with a fresh glass pipet and dispersing the aliquot in methanol (5 mL). The resulting dispersion was centrifuged for ca. 2 min, the supernatant discarded, and the precipitate redispersed in toluene (4 mL). Collection of aliquots continued for 70−100 min. Reliable kinetic data could be obtained up to the initial signs of sedimentation, which was indicated by the appearance of a brown film on the sides of the flask.

**Collection of Precursor-Disappearance Data.** Trials were run to monitor the disappearance of the precursor as a function of time. For each, a nanoparticle-growth mixture was prepared and heated as described above. Aliquots (1.0 mL) of the heated mixture were taken at specific time intervals and dispersed in ice-cold $d_6$-acetone (2.0 mL) to immediately quench the reaction. $^{31}P\{^1H\}$ NMR spectra were obtained from these samples at room temperature with a pulse delay of 5 s. The precursor and byproduct peaks were integrated, and from those integrals the fraction of remaining precursor was calculated. The natural log of the precursor fraction was plotted as a function of time, and from the plot the order and the half-life for the precursor disappearance were determined.

**Measurement of Nanocrystal Size and Size Distribution.** TEM specimens were prepared by dipping carbon-coated copper grids into the toluene solution and allowing them to dry in air. Images taken at 500 K magnification were saved in the TIF format and resampled using Image-Pro Express software (version 4.5). Diameter-distribution measurements of particles from the resampled images included 400−750 nanoparticles, taken from different spots on the grid. Using the diameter values measured at different times, and assuming spherical nanoparticle morphologies, nanoparticle volumes were calculated in nm$^3$. These values were used to construct normalized frequency diagrams or crystal-size distributions (CSDs). The volume data were binned using the minimum bin width (5 nm$^3$) that avoided excessive noise or discontinuities in the CSDs.

Similar specimens were also used for high-resolution TEM (HRTEM) studies. Nanoparticles obtained at both early and late times in a kinetic run were examined. The number of particles imaged under HRTEM was significantly less than those counted in low-resolution studies, as these HRTEM studies were primarily for examining nanoparticle crystallinity.

**Kinetics of Ag-nanoparticle Growth Measured by UV−Vis Spectroscopy.** In a typical trial, bis(triphenylphosphine)silver(I) myristate (0.044 g, 0.051 mmol) and AIBN (0.05 g, 0.31 mmol) were dissolved in 4% w/w poly(1-hexadecene)$_{0.67}$-*co*-(1-vinylpyrrolidone)$_{0.33}$ in 1,2-dichlorobenzene (10 mL) in a 50-ml round-bottom flask. The stirred mixture was heated at 130.0 ± 0.1 °C in a 300 mL oil bath connected to an Ace Glass temperature controller. Aliquots (0.1 mL) were taken at specific times and dispersed in 4.0 mL of cyclohexane. The diluted samples were then transferred to 1-cm path-length quartz cuvettes and UV−vis measurements taken. Baseline correction was performed before each measurement.

UV−visible data were reanalyzed using Origin software (version 7.5) by nonlinear least-squares fitting. Before fitting, the data were converted from wavelength (nm) to energy (eV) units, and then fit with a sum of three exponential functions for the background, and one Lorentzian function for the plasmon peak.

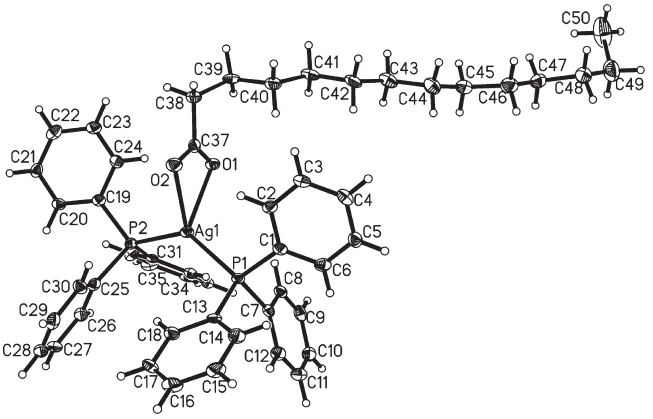


**Figure 1.** Thermal-ellipsoid plot of $[(PPh_3)_2Ag(O_2CC_{13}H_{27})]$. Hydrogen atoms and one of the two unique molecules are omitted for clarity. Selected distances (Å): Ag(1)−P(1), 2.4115(10); Ag(1)−P(2), 2.4292 (10); Ag(1)−O(1), 2.384(3); Ag(1)−O(2), 2.497(3). Selected angles (deg): O(1)−Ag(1)−P(1), 114.72(7); O(1)−Ag(1)−P(2), 104.88(7); P(1)−Ag(1)−P(2), 134.22(4); O(1)−Ag(1)−O(2), 53.86(9); P(1)−Ag(1)−O(2), 110.60(7); P(2)−Ag(1)−O(2), 110.94(7).

The sum of the three fitted exponentials was then subtracted from the data and the resulting background-subtracted data refitted by a Lorentzian function. The height of this Lorentzian was determined as a function of time as nanoparticle growth proceeded.

Separately, a calibration curve was constructed for correlating the height of the Lorentzian-fitted plasmon peak with the mean diameter of Ag nanoparticles. Nanoparticles were harvested from similar kinetic trials at various times and their mean diameters determined by analysis of TEM images (see above). The UV−vis spectra of these specimens were recorded, and subjected to the fitting procedure described above. Mean diameter vs plasmon-peak (Lorentzian) height was then plotted as a calibration curve, allowing nanoparticle mean diameter in the kinetic trials to be extracted from the UV−vis data.

**Crystallographic Procedures.** Crystals of $[(PPh_3)_2Ag(O_2CC_{13}H_{27})]$ suitable for X-ray structure determination were grown from a concentrated benzene solution at room temperature over a 24 h period. A specimen having dimensions of $0.35 \times 0.22 \times 0.08$ mm$^3$ was selected for analysis. A Bruker APEXII Kappa Charge Coupled Device (CCD) Detector system single-crystal X-ray diffractometer with graphite monochromated Mo Kα radiation ($\lambda$ = 0.71073 Å) was used for the preliminary examination and data collection. Final data collection and data integration were performed using APEX2 and SAINT software packages (Bruker Analytical X-ray, Madison, WI, 2007). Cell constants were determined by a global refinement of xyz centroids of 9977 reflections. Structure solution and refinement were carried out using the SHELXTL-PLUS software package. Direct methods were used to solve the crystal structure and full matrix least-squares methods used for the refinement. The hydrogen atoms were treated using appropriate riding model (AFIX m3). Of the two unique molecules in the asymmetric unit one showed disorder in the aliphatic chain of the myristate ligand. The disorder was resolved with partial-occupancy atoms for C96 through C99 (58:42%) and refined with geometrical and thermal parameter restraints.

A projection view of the molecule with non-hydrogen atoms represented by 50% thermal ellipsoids, and showing the atom labeling is given in Figure 1. Crystallographic data and structure parameters are listed in Table 1. The CCDC reference number for $[(PPh_3)_2Ag(O_2CC_{13}H_{27})]$ is 770942. Structure-factor tables are available from the authors in electronic format.

**Table 1. Crystal Data and Structure Refinement for $[(PPh_3)_2Ag(O_2CC_{13}H_{27})]$**

| | |
|---|---|
| empirical formula | $C_{50}H_{57}AgO_2P_2$ |
| formula weight | 859.77 |
| temperature (K) | 100(2) |
| wavelength (Å) | 0.71073 |
| cryst syst | triclinic |
| space group | $P\bar{1}$ |
| $a$ (Å) | 11.9265(8) |
| $b$ (Å) | 13.3115(10) |
| $c$ (Å) | 29.1762(19) |
| α (deg) | 102.653(4) |
| $\beta$ (deg) | 95.209(4) |
| $\gamma$ (deg) | 103.926(4) |
| $V$ (Å$^3$) | 4336.0(5) |
| $Z$ | 4 |
| density (calcd) (Mg/m$^3$) | 1.317 |
| absorp coeff (mm$^{-1}$) | 0.577 |
| $F$(000) | 1800 |
| cryst size (mm$^3$) | 0.35 × 0.22 × 0.08 |
| $\theta$ range for data collection (deg) | 1.78−25.00 |
| index ranges | $-14 \le h \le 14$, $-15 \le k \le 15$, $-34 \le l \le 34$ |
| no. of reflns collected | 132 913 |
| no. of independent reflns | 15 143 [$R$(int) = 0.079] |
| completeness to $\theta$ = 25.00° | 99.0% |
| absorp corr | semiempirical from equivalents |
| max and min transmission | 0.9553 and 0.8235 |
| refinement method | full-matrix least-squares on $F^2$ |
| data/restraints/params | 15143/104/1010 |
| GOF on $F^2$ | 1.056 |
| final $R$ indices [$I > 2\sigma(I)$] | $R_1$ = 0.0514, $wR_2$ = 0.1128 |
| $R$ indices (all data) | $R_1$ = 0.0759, $wR_2$ = 0.1228 |
| largest diff. peak and hole (e Å$^{-3}$) | 1.063 and −1.461 |

## Results

**Precursor Synthesis and Characterization.** Bis(triphenylphosphine)silver(I) myristate $[(PPh_3)_2Ag(O_2CC_{13}H_{27})]$ was obtained in high yield according to eq 1. To the best of our knowledge, $[(PPh_3)_2Ag(O_2CC_{13}H_{27})]$ is a new compound; however, the related bis(triphenylphosphine)-silver(I) stearate was previously reported by Whitcomb and co-workers.[33] Bis(triphenylphosphine)silver(I) myristate is a colorless solid that is soluble in organic solvents, is not light sensitive, and may be safely stored and manipulated under ambient air at room temperature for at least 2 years.

$$2PPh_3 + Ag(O_2CC_{13}H_{27}) \rightarrow (PPh_3)_2Ag(O_2CC_{13}H_{27}) \quad (1)$$

The molecular structure of $[(PPh_3)_2Ag(O_2CC_{13}H_{27})]$ determined crystallographically is shown in Figure 1. It is isostructural with the analog synthesized by Whitcomb and co-workers.[33] The molecular unit is mononuclear with a four-coordinate silver atom in a distorted-tetrahedral coordination environment. The myristate ligand is bidentate. Key bond distances and angles are summarized in the caption to Figure 1. The crystallographic data are recorded in Table 1. Additional structural data are provided in Tables S1−S5 in the Supporting Information.

The low-temperature $^{31}P\{^1H\}$ NMR spectrum of $[(PPh_3)_2Ag(O_2CC_{13}H_{27})]$ in $d_6$-acetone (−80 °C) consisted of two doublets (Figure 2), corresponding to two ($^{107}$Ag and $^{109}$Ag) isotopomers in near-equal amounts. The abundant isotopes of Ag are $^{107}$Ag (51.82%) and $^{109}$Ag (48.18%), and both have nuclear spins of $I$ = 1/2. Two doublets with very similar chemical shifts of 8.63 and 8.64 ppm, respectively, were thus observed. The P−Ag coupling constants were also similar: $^1J$ (P, $^{109}$Ag) = 471.98 Hz, and $^1J$ (P, $^{107}$Ag) = 414.13 Hz. The ratio $^1J$ ($^{107}$Ag $^{31}$P):$^1J$ ($^{109}$Ag$^{31}$P) was 0.877, which agrees with the ratio of gyromagnetic ratios, $\gamma$($^{107}$Ag):$\gamma$($^{109}$Ag) = 0.870.[34−36]

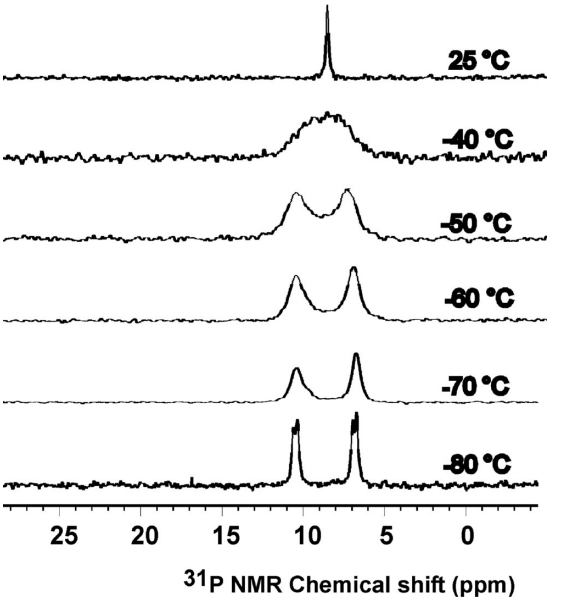


**Figure 2.** Variable-temperature $^{31}P\{^1H\}$ NMR spectra of $[(PPh_3)_2Ag(O_2CC_{13}H_{27})]$ in $d_6$-acetone.

$^{31}P\{^1H\}$ NMR spectra recorded at various temperatures between −80 and 25 °C are shown in Figure 2. The two doublets observed at −80 °C coalesced into a single resonance at −40 °C, and further sharpened at room temperature. Similar coalescence behavior was observed previously for other silver−phosphine complexes,[34,37] and was attributed to a dissociative equilibrium that exchanges bound and free phosphine ligands and therefore collapses the P−Ag $J$ coupling.

**Silver Nanoparticle Formation.** Silver nanoparticles were produced by reaction of the silver precursor and AIBN in solution (130 °C) in the presence of poly(1-hexadecene)$_{0.67}$ - co- (1-vinylpyrrolidone)$_{0.33}$ (PHD-co-PVP)[38,39] as a polymer stabilizer. Nanoparticle formation was monitored by UV−visible spectroscopy. A peak emerged in the extinction spectrum (Figure 3) at $\lambda_{max}$ = 420 nm, which shifted toward $\lambda_{max}$ = 409 nm and grew in

(33) Whitcomb, D. R.; Rogers, R. D. *J. Chem. Crystallogr.* **1996**, *26*, 99–105.
(34) Santini, C.; Lobbia, G. G.; Pettinarari, C.; Pellei, M.; Valle, G.; Calogero, S. *Inorg. Chem.* **1998**, *37*, 890–900.
(35) Attar, S.; Alcock, N. W.; Bowmaker, G. A.; Frye, J. S.; Bearden, W. H.; Nelson, J. H. *Inorg. Chem.* **1991**, *30*, 4166–4176.
(36) Liu, C. W.; Pan, H.; Fackler, J. P.; Wu, G.; Wasylishen, R. E.; Shang, M. *J. Chem. Soc., Dalton Trans.* **1995**, 3691–3697.
(37) Muetterties, E.; Alegranti, C. W. *J. Am. Chem. Soc.* **1972**, *94*, 6388–6391.
(38) Wang, F.; Tang, R.; Yu, H.; Gibbons, P. C.; Buhro, W. *Chem. Mater.* **2008**, *20*, 3656–3662.
(39) Wang, F.; Buhro, W. E. *Small* **2010**, *6*, 573–581.

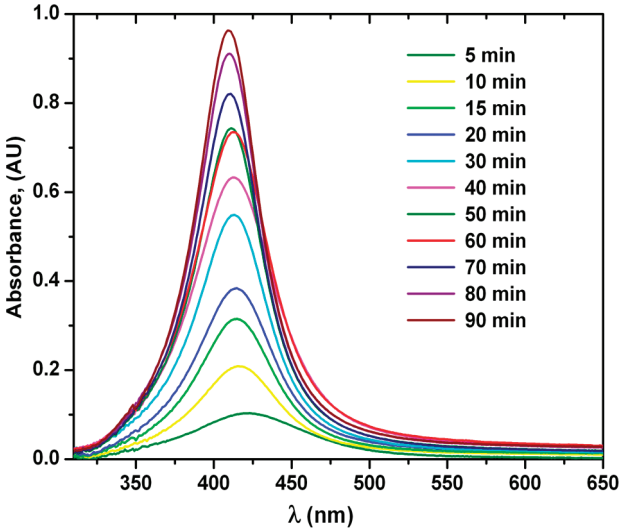


**Figure 3.** UV−visible exctinction spectra of Ag nanoparticles after background subtraction (see Experimental Section). The spectra were collected at various times during a growth trial as indicated in the inset.

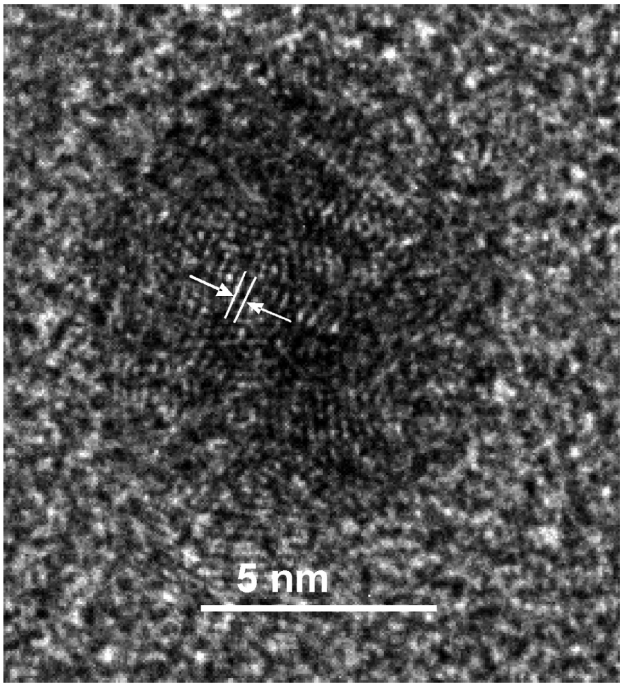


**Figure 4.** HRTEM image of a polycrystalline Ag nanoparticle showing a $d_{111}$ lattice spacing of 0.25 ± 0.06 nm. The scale bar is 5 nm.

intensity over the course of the growth period (80−90 min). This peak is consistent with the surface-plasmon resonance of Ag nanoparticles in the size range of 1−15 nm.[40−42] TEM images confirmed the formation of small nanoparticles at early times, which evolved into larger nanoparticles as growth proceeded (see below). Energy-dispersive X-ray spectroscopy on the nanoparticles

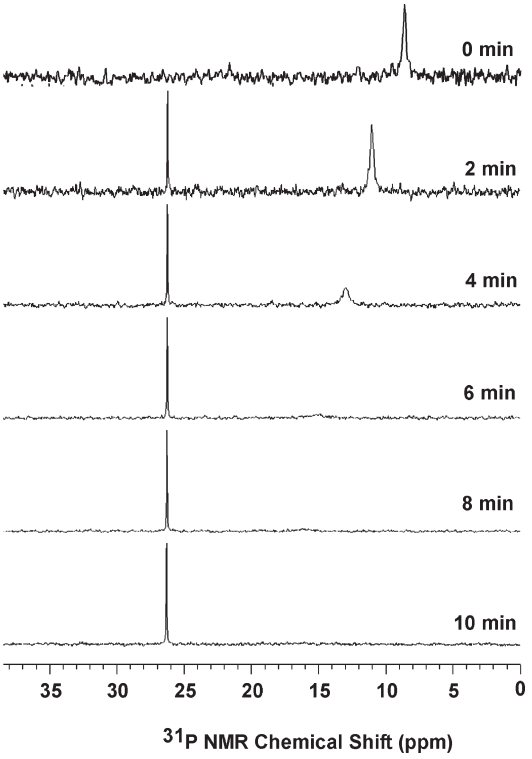


**Figure 5.** $^{31}P\{^{1}H\}$ NMR spectra taken at various times during the decomposition of $[(PPh_3)_2Ag(O_2CC_{13}H_{27})]$ at 130 °C. The precursor resonance (8.7 ppm) disappears as the product $Ph_3P{=}O$ resonance (26.2 ppm) appears.

confirmed their elemental Ag composition (Figure S1). Lattice spacings measured from HRTEM images (0.25 ± 0.06 nm, Figure 4) were consistent with $d_{111}$ in fcc Ag (0.24 nm according to ICDD-PDF #01−071−3762).

**Reaction Monitoring.** The phosphorus byproduct of Ag-nanoparticle formation was identified by $^{31}P\{^{1}H\}$ NMR monitoring. Spectra obtained over the course of the reaction revealed the disappearance of the Ag precursor resonance at 8.7 ppm with the appearance of a product resonance at 26.2 ppm (Figure 5). The product resonance was shown to correspond to the phosphine oxide $Ph_3P{=}O$ by independent measurement of the spectrum of authentic $Ph_3P{=}O$ under identical conditions. Additionally, authentic $Ph_3P{=}O$ was spiked into a reaction mixture, upon which the intensity of the product resonance at 26.2 ppm was increased.

The organic byproduct of the reaction was established by electrospray-ionization mass spectrometry (ESI-MS) and $^{13}C\{^{1}H\}$ NMR. To obtain appropriate specimens for these analyses, the Ag-generating reaction described above was conducted on a larger scale and in the absence of the PHD-co-PVP polymer stabilizer. The reaction mixture was decanted, the solvent was evaporated, and the residue was analyzed. The base peak in the ESI-MS (see Figure S2 in the Supporting Information) corresponded to $m/z$ = 279 amu. The $^{13}C\{^{1}H\}$ NMR spectrum (see Figure S3 in the Supporting Informaiton) contained the characteristic resonances for the hydrocarbon chain for the myristyl group, and resonances assigned to cyano (CN, 122.0 ppm) and carbonyl (CO, 180.7 ppm) carbon

(40) Kreibig, U. *J. Phys. F: Metal Phys.* **1974**, *4*, 999–1014.
(41) Hövel, H.; Fritz, S.; Hilger, A.; Kreibig, U. *Phys. Rev. B.* **1993**, *48*, 18178–18188.
(42) Van Hyning, D. L.; Klemperer, W. G.; Zukoski, C. F. *Langmuir* **2001**, *17*, 3120–3127.
(43) Kimling, J.; Maier, M.; Okenve, B.; Kotaidis, V.; Ballot, H; Plech, A. *J. Phys. Chem. B* **2006**, *110*, 15700–15707.

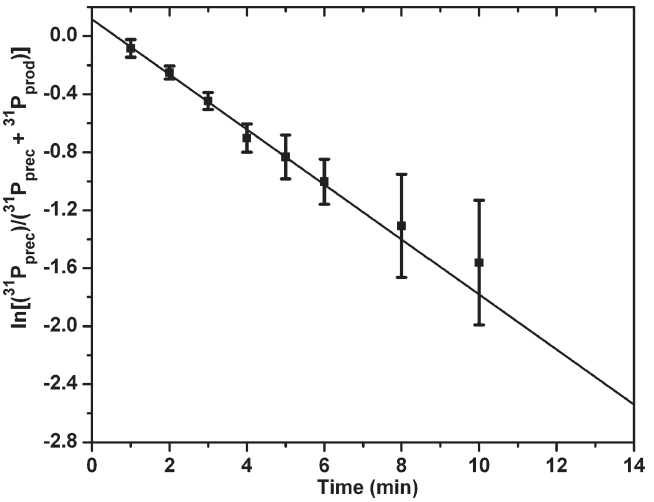


**Figure 6.** Plot of the natural log of the integrated $^{31}P$ NMR precursor intensity divided by the total integrated $^{31}P$ NMR intensity vs time for $[(PPh_3)_2Ag(O_2CC_{13}H_{27})]$ disappearance by eq 2.

atoms. The results indicated that the organic byproduct was compound **I** (MW = 279 g/mol, eq 2), resulting from the coupling of fragments derived from the myristate ligand and AIBN. The reaction stoichiometry in eq 2 was therefore identified.

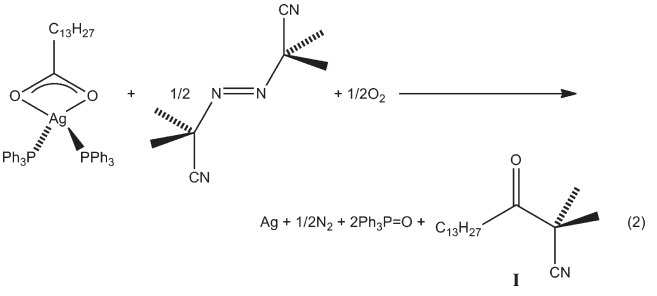


As a control experiment, Ag-nanoparticle growth was conducted as described in the section above, except in a nitrogen-sparged solution and under a nitrogen atmosphere, rather than under ambient air. The progress of nanoparticle growth, which was monitored by UV−visible spectroscopy, was significantly inhibited under these conditions. After a growth period of 50 min, the Ag-nanoparticle plasmon feature was extremely broad and scarcely detectable, establishing that the nanoparticle mean size was well below 3 nm, a size achieved under normal conditions within 3−5 min (see below). We attributed this inhibition to the lack of the $O_2$ necessary to support eq 2.

A kinetics study of precursor disappearance according to eq 2 was conducted at 130.0 ± 0.1 °C, under air and with a 12-fold excess of AIBN. $^{31}P\{^1H\}$ NMR data like those in Figure 5 were integrated to provide quantitative measures of precursor remaining and $Ph_3P{=}O$ product formed (the spectra shown in Figure 5 constitute a partial set). Precursor disappearance was plotted as the natural log of the integrated precursor resonance ($^{31}P_{prec}$) divided by the total integrated area of the precursor and product resonances ($^{31}P_{prec}$ + $^{31}P_{prod}$) vs time, $\ln[(^{31}P_{prec})/(^{31}P_{prec} + {}^{31}P_{prod})]$ vs $t$ (Figure 6). The plot was linear over

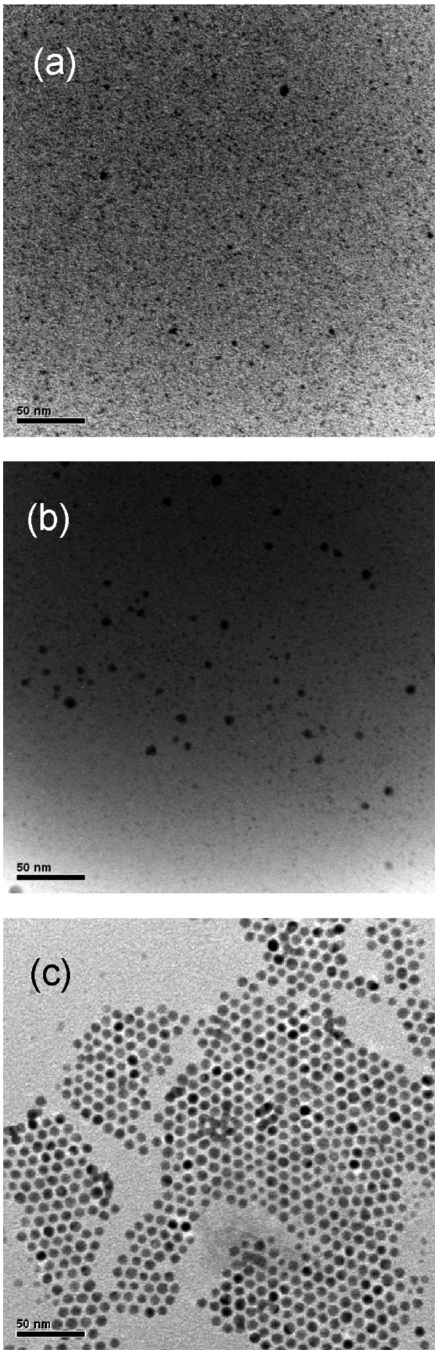


**Figure 7.** TEM images obtained at various stages of Ag-nanoparticle growth. (a) After 3 min, (b) after 5 min, and (c) after 55 min.

approximately 3 half-lives, establishing pseudo first-order kinetics for the disappearance of $[(PPh_3)_2Ag(O_2CC_{13}H_{27})]$. A rate constant of 0.190 ± 0.022 $min^{-1}$ was obtained, yielding a half-life of 3.65 ± 0.42 min. This quantitative value will be used below in the determination of the mechanism of nanoparticle growth, and will rule out a classical, LaMer-type mechanism as the predominant nanoparticle growth mechanism.

**Early Time Particle Growth Monitoring.** Nanoparticle growth was monitored by removing aliquots for TEM analysis from kinetics runs conducted at 130.0 ± 0.1 °C (eq 2). A distribution of small nanoparticles having diameters of 1.8 ± 0.6 nm was observed to emerge at

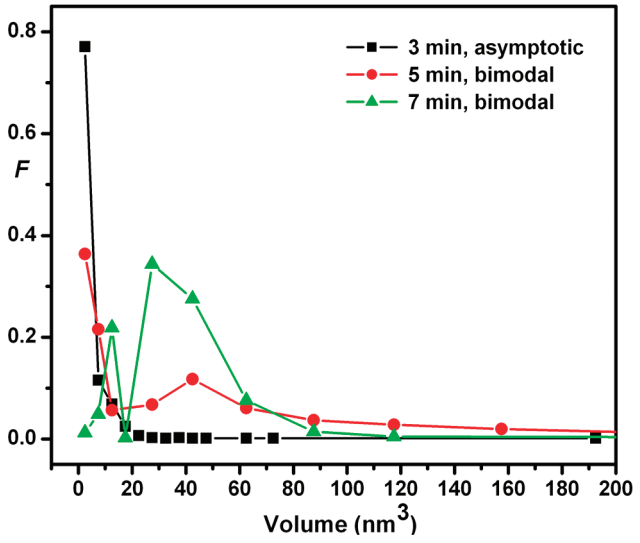


**Figure 8.** CSDs determined in a Ag-nanoparticle growth trial at 3 min (black), 5 min (red), and 7 min (green). The plots show the evolution of the CSDs from asymptotic to bimodal. The fraction $F$ of the nanoparticles in a given volume bin is plotted against nanoparticle volume.

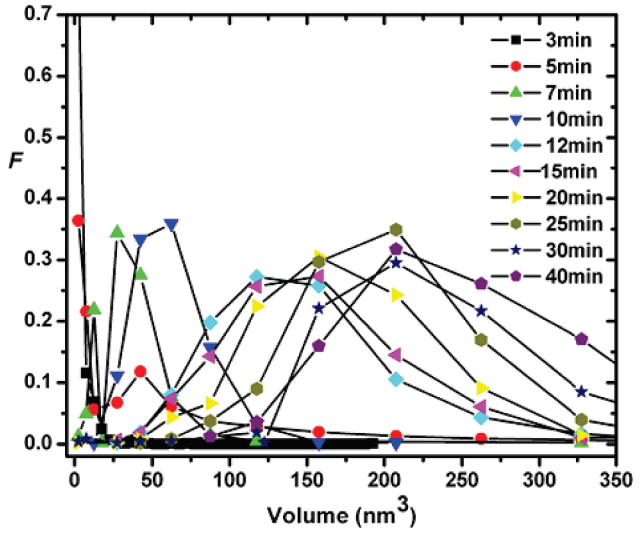


**Figure 9.** Extensive series of CSDs determined at various times (inset) in a Ag-nanoparticle growth trial, including the three plots shown in Figure 8. The fraction $F$ of nanoparticles in a given volume bin is plotted against nanoparticle volume.

reaction times as short as 3−4 min (Figure 7a). We refer to these small nanoparticles as primary nanocrystals. TEM images of aliquots taken just a few minutes later revealed a population of distinctly larger nanoparticles interspersed with the primary nanocrystals (Figure 7b); that is, the crystal-size distribution (CSD) evolved from asymptotic to bimodal (Figure 8). We note that contrast limitations in the images of the bimodal distributions precluded a complete count of the remaining primary nanocrystals, which were difficult to discern in the presence of the larger nanoparticles. In time, the primary nanocrystals disappeared as the larger nanoparticles continued to grow, reaching a mean size of 7.3 ± 0.7 nm after 50−60 min (Figure 7c).

HRTEM studies were undertaken to determine the crystallinity of the larger nanoparticles. Images were

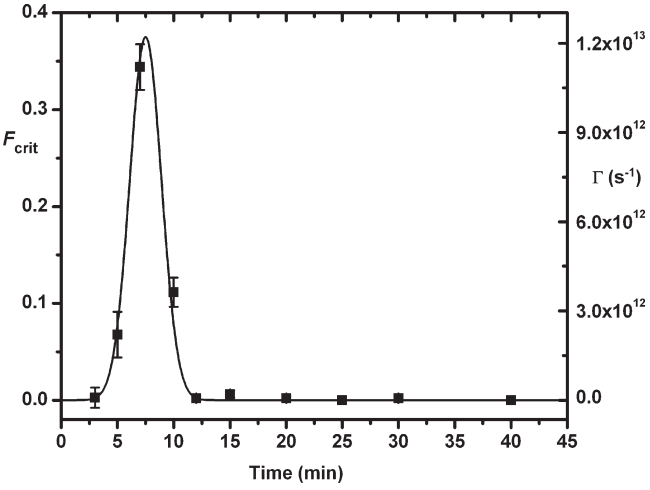


**Figure 10.** Aggregative-nucleation function (Gaussian fit) for Ag-nanoparticle growth under the conditions described in the text. The left and right axes correspond to the critical-aggregate fraction $F_{crit}$ and the scaled nucleation rate $\Gamma(t)$, respectively (see text).

obtained of both smaller (but not primary) nanoparticles from early times, and larger nanoparticles from later times (Figure 4). The vast majority of the nanoparticles examined were polycrystalline, as shown in Figure 4, which is consistent with an aggregative growth process involving aggregation and coalescence of primary nanocrystals.[6,16,21,31,32,44,45]

**Determination of the Aggregative-Nucleation Function.** A more-extensive set of CSDs obtained from a kinetics trial is given in Figure 9. The bimodality observed in the early time CSDs is primary evidence of nanoparticle aggregation.[17−21,26−28] We have previously found that aggregative growth may be a nucleation-driven process, requiring the formation of a critical aggregate of primary nanocrystals to initiate further aggregative growth. Because the primary nanocrystals resulted from a classical nucleation and growth, the aggregative-nucleation process constitutes a second nucleation event.

We and others have shown that a peak emerges in the CSD at the critical-nucleus size (evident at 5 min in Figure 9), which subsequently shifts to progressively larger size. This emergent peak results from a burst of nucleation, corresponding to a rapidly increasing nucleation rate.[28,46−50] In aggregative growth, the nucleation corresponds to the formation of critical-sized aggregates, which coalesce and subsequently grow by addition of primary nanocrystals.[21] The nucleation rate then falls off as growth ensues. Consequently, the nucleation function−the time dependence of the aggregative-nucleation

(44) Polte, J.; Ahner, T.; Delissen, F.; Sokolov, S.; Emmerling, F.; Thünemann, A.; Kraehnert, R. *J. Am. Chem. Soc.* **2010**, *132*, 1296–1301.
(45) Polte, J.; Erler, R.; Thünemann, A; Sokolov, S.; Ahner, T.; Rademann, K.; Emmerling, F.; Kraehnert, R. *ACS Nano* **2010**, *4*, 1076–1082.
(46) Dixit, N. M.; Zukoski, C. F. *Phys. Rev. E* **2002**, *66*, 125602.
(47) Gusak, A. M.; Hodaj, F.; Bogatyrev, A. O. *J. Phys.: Condens. Matter* **2001**, *13*, 2767–2787.
(48) Talukdar, S. S.; Swihart, M. T. *J. Aerosol Sci.* **2004**, *35*, 889–908.
(49) Lümmen, N.; Kraska, T. *J. Aerosol Sci.* **2005**, *36*, 1409–1426.
(50) Mukherjee, D.; Prakash, A.; Zachariah, M. R. *J. Aerosol Sci.* **2006**, *37*, 1388–1399.

rate $\Gamma(t)$—first rises, passes through a maximum $\Gamma_{max}$, and then decays (see below).

The critical-aggregate size, expressed as a volume $V_{crit}$, was revealed by Figure 9 (5 min) to be $27.5 \pm 2.5$ nm$^3$, or 10 (1.7-nm-diameter) primary nanocrystals, corresponding to an effective diameter of 3.9 nm for the coalesced critical aggregate. This $V_{crit}$ value was used[21] to construct the nucleation function as follows. The fraction $F_{crit}$ of nanoparticles in the CSDs having the critical size $V_{crit}$ was plotted vs time (Figure 10). The $F_{crit}$ data were fitted with the Gaussian profile in eq 3, where $t$ is time, $\Delta t_n$ is the $2\sigma$ width of the Gaussian, $\tau_n$ is the time at the Gaussian maximum, and A is the area under the Gaussian (all in min). The Gaussian was scaled as the nucleation function $\Gamma(t)$ by setting $A$ (in eq 3) equal to $N$, the number of critical aggregates formed, and by calculating $\Gamma_{max}$ from eq 4.[21] The quantity $N$ was estimated from the mean final nanoparticle volume and the total amount of Ag as previously described.[21] The time at the maximum aggregative-nucleation rate $\Gamma_{max}$ and the width of the time window for aggregative nucleation were determined to be $\tau_n = 7.50 \pm 0.29$ min and $\Delta t_n = 2.80 \pm 0.32$ min, respectively, by the eq 3 fit. These quantities provide measures of the time scale for aggregative nucleation, and are used below to characterize the growth mechanism.

$$F_{crit}(t) = \frac{A}{\Delta t_n \sqrt{\frac{\pi}{2}}} \exp\left[-\frac{2(t-\tau_n)^2}{\Delta t_n{}^2}\right] \quad (3)$$

$$\Gamma_{max} = \frac{N}{\Delta t_n \sqrt{\frac{\pi}{2}}} \quad (4)$$

**Measurement of Particle Growth Kinetics.** The time evolution of the Ag-nanoparticle mean volume was followed by both TEM and UV−visible spectroscopy. However, because the TEM CSDs were obtained by counting only 400−750 nanoparticles, whereas the UV−visible analyses effectively measured the entire nanoparticle populations, the UV−visible data were considered to provide a statistically more-reliable measure of the nanoparticle mean size. Consequently, the nanoparticle growth kinetic profiles were composed primarily of UV−visible data.

Calibration plots were constructed to relate TEM-determined mean diameters with the height of the plasmon resonance in the corresponding UV−visible spectra. These plots used the TEM and UV−visible data collected from five separate kinetics trials. As described in the Experimental Section, the plasmon-feature height was extracted from the UV−visible extinction spectra by background subtraction and Lorentzian fitting. The plots of TEM mean diameter (in nm) vs plasmon-feature height (in absorbance units) were empirically linear (see Figure S4 in the Supporting Information). The slopes and intercepts extracted by least-squares fitting were averaged

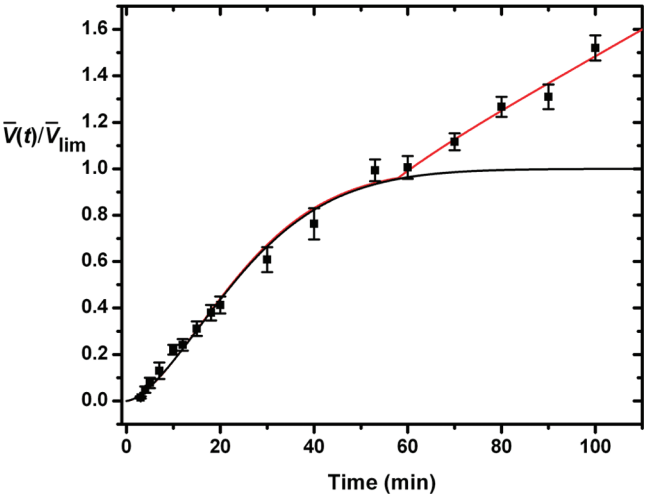


**Figure 11.** Kinetic data and the eq 6 fit (red curve) for Ag-nanoparticle growth. The black curve plots the first term only from the eq 6 fit. $\bar{V}(t)$ is the time-dependent nanoparticle mean volume, and $\bar{V}_{lim}$ is the mean volume at the end of active growth (at 60 min).

to give eq 5, where $\bar{d}$ is the mean diameter and $A$ is absorbance (extinction). Mean nanoparticle diameters determined from the UV−visible data with eq 5 were converted to mean volumes for the kinetic analyses by assuming spherical morphologies.

$$\bar{d}(\text{nm}) = (5.41 \pm 0.37)A \text{ (in abs units)} + (3.34 \pm 0.35) \quad (5)$$

A representative kinetic profile for Ag-nanoparticle growth is given in Figure 11. The data are plotted as $\bar{V}(t)/\bar{V}_{lim}$ vs time, where $\bar{V}(t)$ is the mean nanoparticle volume and $\bar{V}_{lim}$ is the limiting mean volume at the end of the active-growth period (see below; $1/\bar{V}_{lim}$ is a merely scaling factor). Figure 11 includes both TEM and UV−visible data; however, the UV−vis data were used in the kinetic fits discussed below, except for the time points at which the mean nanoparticle diameters were below 3 nm. We found that nanoparticles having diameters below about 3 nm did not produce readily discernible plasmonic features. Thus the $\bar{V}(t)/\bar{V}_{lim}$ data for time points earlier than 5 min were determined from TEM data. As revealed by Figure 11, the kinetic plots exhibited a pseudosigmoidal profile, which is further analyzed below.

Nanoparticle growth kinetics often exhibit a sigmoidal profile resembling that in Scheme 1.[13,22−25,30,51−53] The initial induction period is associated with the nucleation process, which is followed by a rapid nanoparticle-size increase associated with the active-growth regime. At the end of active growth a plateau occurs in the kinetic profile, until the onset of Ostwald ripening. In our case, aggregative nucleation began so early (3 min; see Figure 10) that the initial induction period was not observed.

(51) Talapin, D. V.; Rogach, A. L.; Haase, M.; Weller, H. *J. Phys. Chem. B.* **2001**, *105*, 12278–12285.
(52) Hiramatsu, H.; Osterloh, F. E. *Chem. Mater.* **2004**, *16*, 2509–2511.
(53) Skrdla, P. J.; Robertson, R. T. *Chem. Mater.* **2008**, *20*, 3–4.

Furthermore, Ostwald ripening began shortly after the end of the aggregative-growth regime, such that the final plateau extended for only about 7 min prior to the onset of further growth by Ostwald ripening (see below). Consequently, we describe the kinetic profile as pseudosigmoidal.

We[21] and others[53] have shown that sigmoidal nanoparticle-growth profiles are in some cases well fit by a KJMA model. However, we found a simple KJMA equation unable to fit the rising slope in the Figure 11 data at later times. We attributed this late-time nanoparticle growth to Ostwald ripening, which is known to produce a linear increase in mean particle volume with time.[12,54−56] Additionally, the conditions favorable to Ostwald ripening require the depletion of the growth nutrient,[51,57−60] which in this case was primary Ag nanocrystals. Consequently, one expects the onset of Ostwald ripening after the conclusion of the active-growth regime.

The Figure-11 data were fit by a modified KJMA expression (eq 6) to determine the time for the onset of Ostwald ripening ($\tau_{OR}$). Equation 6 consists of two terms, the first of which is a standard KJMA term to fit nucleation and active growth, where $k_g$ ($min^{-1}$) is a rate parameter and $n$ the Avrami exponent.[21] The second term provides a linear increase in mean volume to account for Ostwald ripening.[54−56] The rate parameter for Ostwald ripening $k_{OR}$ ($min^{-1}$) is multiplied by a logistic, "turn-on" function to activate Ostwald ripening at a time $\tau_{OR}$ (min). The time width $w$ of the turn-on function was arbitrarily chosen to be 2 min. Thus, the fitting parameters were $k_g$, $n$, $k_{OR}$, and $\tau_{OR}$, with the fitted value of $\tau_{OR}$ being of primary interest.

$$\frac{\bar{V}(t)}{\bar{V}_{lim}} = (1-\exp(-k_g t)^n) + \left[\frac{(t-\tau_{OR})}{1+\exp(-2w(t-\tau_{OR}))}\right]k_{OR} \quad (6)$$

Two curves are plotted in Figure 11. The red curve is the full eq 6 fit, and the black curve plots the first, KJMA term only. The primary difference is that the red curve tracks the Ostwald ripening at later times, whereas the black curve levels off at the conclusion of the active (aggregative) growth regime. The value of $\tau_{OR}$ determined from the eq 6 fit was 57.9 ± 3.4 min, indicating that Ostwald ripening began at that time.

We next sought to determine the start time for Ostwald ripening by a second quantitative measure. Prior studies elsewhere have shown that the CSD narrows during the active-growth regime,[51,57,60] including by aggregative growth,[18] and reaches its minimum value at the conclusion of active, nutrient-supported growth. The nanoparticle mean siz then remains nearly constant for a period as the CSD begins to spontaneously broaden,[51,57,60,61] initiating Ostwald ripening, which is facilitated by a broadened CSD. Therefore, after a rest period, the mean size begins to increase by Ostwald ripening. Such a rest period is evident in Figure 11 in the range of approximately 53−60 min. Conventional Ostwald ripening progressively broadens the CSD, and so the onset of this broadening provides a second measure of the onset time for Ostwald ripening.[51,57,60]

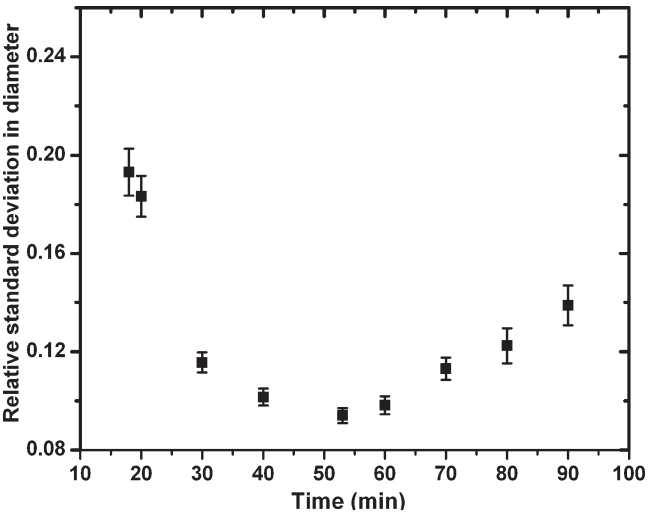


**Figure 12.** Plot of relative standard deviation in the nanoparticle CSD vs time. The plot passes through a minimum before starting to rebroaden, indicating the end of aggregative growth and the onset of Ostwald ripening. The relative standard deviation is the standard deviation in the diameter divided by the nanoparticle mean diameter.

The relative standard deviation in the Ag-nanoparticle CSD during a growth trial is plotted in Figure 12. The CSD was observed to initially narrow, and achieve a minimum value at 53 min. Subsequently, the CSD rebroadened. The onset of this rebroadening was estimated from the Figure 12 data to be 60 ± 5 min, in remarkable agreement with the value of $\tau_{OR}$ = 57.9 ± 3.4 min (see above). Consequently, the onset of Ostwald ripening was determined to be 58−60 min by two independent quantitative measures.

## Discussion

**Precursor-Decomposition Chemistry.** The Ag-generating reaction in eq 2 was developed by us empirically. Silver carboxylates decompose thermally to elemental Ag, and have been used in photothermographic applications[62−65] and to deposit Ag films by CVD[66−69] and ALD.[70] Prior

(54) Lifshitz, I. M.; Slyozov, V. V. *J. Phys. Chem. Solids*. **1961**, *19*, 35–50.
(55) Chen, M. K.; Voorhees, P. W. *Modelling Simul. Mater. Sci. Eng.* **1993**, *1*, 591–612.
(56) Vorhees, P. W. *Annu. Rev. Mater. Sci.* **1992**, *22*, 197–215.
(57) Sagui, C.; O'Gorman, D. S.; Grant, M. *Phys. Rev. E.* **1997**, *56*, R21–R24.
(58) Park, J.; Joo, J.; Soon, G. K.; Jang, Y.; Hyeon, T. *Angew. Chem., Int. Ed.* **2007**, *46*, 4630–4660.
(59) McKay, M. R.; Venables, J. A.; Drucke, J. *Solid State Commun.* **2009**, *149*, 1403–1409.
(60) Mantzaris, N. V. *Chem. Eng. Sci.* **2005**, *60*, 4749–4770.
(61) Chen, Y.; Johnson, E.; Peng, X. *J. Am. Chem. Soc.* **2007**, *129*, 10937–110947.
(62) Bokhonov, B. B.; Burleva, L. P.; Whitcomb, D. R.; Usanov, Y. E. *J. Imaging Sci.Technol.* **2001**, *45*, 259–266.
(63) Maekawa, T.; Yoshikane, M.; Fujimura, H.; Toya, I. *J. Imaging Sci. Technol.* **2001**, *45*, 365–372.
(64) Sahyun, M. R. V. *J. Imaging Sci.Technol.* **2005**, *49*, 337–347.
(65) Olson, L. P.; Whitcomb, D. R.; Rajeswaran, M.; Blanton, T. N.; Stwertka, B. J. *Chem. Mater.* **2006**, *18*, 1667–1674.

reports of Ag-nanoparticle formation from Ag-carboxylate precursors also exist.[71,72]

We found that the precursor $[(PPh_3)_2Ag(O_2CC_{13}H_{27})]$ decomposed only very slowly at 130 °C in *o*-dichlorobenzene solvent and in the presence of the polymer stabilizer. However, at 150 °C under the same conditions, the decomposition was extremely rapid and the resulting Ag nanoparticles exhibited broad size distributions. Several studies have suggested that Ag carboxylates decompose by radical pathways,[68,73,74] and so we attempted to accelerate Ag-nanoparticle formation at 130 °C by the addition of the radical initiator AIBN.

In our initial efforts, we added small, substoichiometric quantities of AIBN to the precursor mixture. Some Ag nanoparticles were readily generated at 130 °C, but NMR analysis revealed large amounts of unreacted $[(PPh_3)_2Ag(O_2CC_{13}H_{27})]$, even after extended periods. We surmised that the early termination of precursor decomposition indicated a stoichiometric role for AIBN. We ultimately determined that an AIBN/precursor molar ratio of about 6 was necessary for complete conversion to elemental Ag, and elucidated the eq 2 stoichiometry as described in the Results section.

The reaction pathway for eq 2 is not immediately apparent. A C−O bond in the myristate ligand is cleaved, and the remaining fragment is united with the alkyl substituent derived from AIBN in byproduct **I** (eq 2). Both $Ph_3P$ ligands are converted to the oxide $Ph_3P{=}O$. Hints to a possible pathway are provided in a study of the gas-phase thermolysis of $[(n\text{-}Bu_3P)_2Ag(O_2CCF_3)]$ by Kohse-Höinghaus and co-workers.[68] The gas-phase decomposition was monitored by mass spectrometry, and one of the predominant fragments observed corresponded to $[(n\text{-}Bu_3P)_2Ag(O)]^{\cdot+}$ and/or $[(n\text{-}Bu_3P)(n\text{-}Bu_3P{=}O)Ag]^{\cdot+}$ ($m/z$ = 527). That finding suggests to us the pathway outlined in Scheme 2.

In Scheme 2, we propose thermal decomposition of AIBN in an initial step, generating $Me_2(CN)C^{\bullet}$ radicals. Radical attack at the myristate carbonyl carbon atom would produce byproduct **I** and $[(Ph_3P)_2Ag(O)]^{\bullet}$ by ligand fragmentation. The 12-fold excess of AIBN is presumably required because the $Me_2(CN)C^{\bullet}$ radicals may be lost to reactions with the solvent or in other ways, and only a fraction survives to attack the precursor. The $[(Ph_3P)_2Ag(O)]^{\bullet}$ intermediate may rearrange to $[(Ph_3P)(Ph_3P{=}O)Ag]^{\bullet}$, and reoxidize to $[(Ph_3P)(Ph_3P{=}O)Ag(O)]^{\bullet}$. We note that eq 2 is conducted under ambient air and fails to progress when conducted under $O_2$-free conditions (see above). A final rearrangement and ligand dissociation would liberate two equivalents of $Ph_3P{=}O$ and a Ag atom. Scheme 2 accounts for the stoichiometric consumption of AIBN and the necessity of $O_2$, rationalizes all eq 2 reaction products, and is consistent with the available precedent.[68]

**Elucidation of the Nanoparticle Growth Pathway.** The kinetic results for Ag-nanoparticle formation described above establish that classical nucleation and growth, aggregative nucleation and growth, and Ostwald ripening are largely consecutive processes, separated in time from one another. Classical nucleation and growth occurs early, on a time scale that is measured by the half-life for precursor decomposition ($t_{1/2} = 3.65 \pm 0.42$ min). After the rapid, initial formation of small, primary nanocrystals, larger nanoparticles first appear after about 3−4 min (Figure 7a), at which time the $[(PPh_3)_2Ag(O_2CC_{13}H_{27})]$ precursor is half consumed. Figure 10 shows that when the (aggregative) nucleation rate reaches a maximum ($\tau_n = 7.50 \pm 0.29$ min), the precursor is 75% consumed. Figure 11 reveals that the active-growth period extends to 58 min. Thus, 4 half-lives of precursor decomposition (14.6 min), at which point 94% of the precursor has been consumed, occurs within the first 25% of the growth period. Because of the early time scale for precursor decomposition, the LaMer or classical mechanism accounts well for the initial burst of small, primary Ag nanocrystals, but is temporally inconsistent with the extended active-growth regime.

One must next consider if Ostwald ripening can account for the active-growth regime extending to 58 min. However, the observations of pseudosigmoidal growth kinetics, bimodal CSDs at early times, polycrystalline mature nanoparticles, and a second, nonclassical nucleation process are all inconsistent with Ostwald ripening. As noted above, the increase in the mean nanoparticle volume by Ostwald ripening should be linear, not sigmoidal, in time.[12,54−56] As we have discussed extensively previously,[21] Ostwald ripening cannot generate a bifurcated (bimodal) CSD unless a discontinuity in the growth rate occurs at a critical nanoparticle size, resulting from substrate-nanoparticle strain[75] or a nanoparticle morphology transition.[76−79] No such special circumstance exists here. Ostwald ripening of small, primary nanocrystals should produce mature nanoparticles that are single crystals rather than polycrystals.[21,31,32,44,45] Finally, Ostwald ripening is not a nucleation-driven process, and so cannot account for the nucleation behavior evident in Figures 9 and 10. Instead, each of these observations is

(66) Szłyk, E.; Piszczek, P.; Grodzicki, A.; Chaberski, M.; Goliński, A.; Szatkowski, J.; Błaszczyk, T. *Chem. Vap. Deposition* **2001**, *7*, 111–116.
(67) Edwards, D. A.; Harker, R. M.; Mahon, M. F.; Molloy, K. C. *Inorg. Chim. Acta* **2002**, *328*, 134–146.
(68) Haase, T.; Kohse-Höinghaus, K.; Atakan, B.; Schmidt, H.; Lang, H. *Chem. Vap. Deposition* **2003**, *9*, 144–148.
(69) Grodzicki, A.; Łakomska, I.; Piszczek, P.; Szymańska, I.; Szłyk, E. *Coord. Chem.* **2005**, *249*, 2232–2258.
(70) Niskanen, A.; Hatanpää, T.; Arstilä, K.; Leskelä, M.; Ritala, M. *Chem. Vap. Deposition* **2007**, *13*, 408–413.
(71) Lee, D. K.; Kang, Y. S. *ETRI Journal* **2004**, *26*, 252–256.
(72) Uznanski, P.; Bryszewska, E. *J. Mater. Sci.* **2010**, *45*, 1547–1552.
(73) Fields, E. K.; Meyerson, S. *J. Org. Chem.* **1976**, *41*, 916–920.
(74) Busch, K. L.; Cooks, R. G.; Walton, R. A.; Wood, K. V. *Inorg. Chem.* **1984**, *23*, 4093–4097.
(75) Goldfarb, I.; Hayden, P. T.; Owen, J. H. G.; Briggs, G. A. D. *Phys. Rev. B* **1997**, *56*, 10459–10468.
(76) Vine, D. J.; Jesson, D. E.; Morgan, M. J.; Shchukin, V. A.; Bimberg, D. *Phys. Rev. B* **2005**, *72*, 241304(R).
(77) Ross, F. M.; Tersoff, J.; Tromp, R. M. *Microsc. Microanal.* **1998**, *4*, 254–263.
(78) Agnelli, M.; Kolb, M.; Mirodatos, C. *J. Catal.* **1994**, *148*, 9–21.
(79) Takaki, T.; Tomita, Y. *Key Eng. Mater.* **2007**, *340−341*, 1073–1078.

**Scheme 2. Proposed Reaction Pathway for Precursor Decomposition According to eq 2 (see text)**

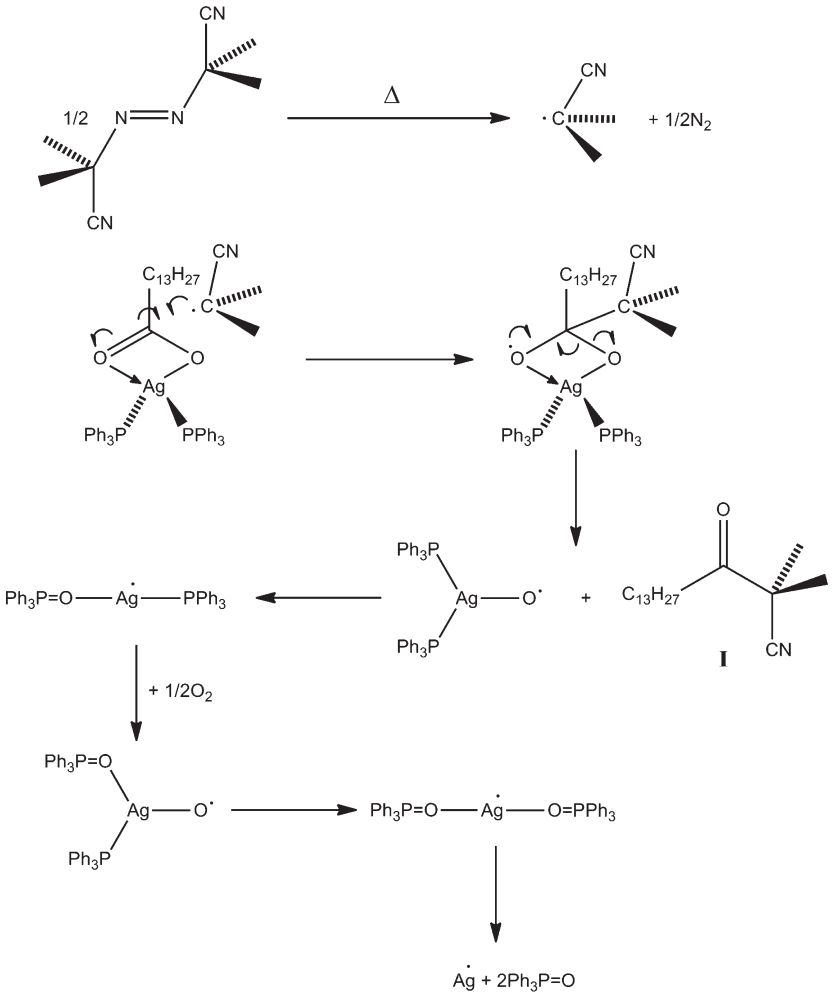


theoretically and experimentally consistent with an aggregative-growth mechanism.[21,46,47,80,81]

We assert that Ostwald ripening begins after the conclusion of the active-growth period at 58 min (see Figure 11). As described in the Results section, two independent measures place the onset of Ostwald ripening at this time: the fitted $\tau_{OR}$ value of 57.9 ± 3.4 min from eq 6, and the time of CSD rebroadening at 60 ± 5 min from Figure 12. Consequently, classical nucleation and growth, aggregative nucleation and growth, and Ostwald ripening all contribute to Ag-nanoparticle growth under the conditions employed, but in different time regimes. The regime of greatest nanoparticle growth is governed by aggregative processes. For synthetic purposes, one would ideally find conditions that eliminate the late-time Ostwald ripening such that the final nanoparticle mean size and size distribution would be fixed at and controlled by the conclusion of the aggregative-growth regime.

**Participation of Aggregative Processes in Nanoparticle Growth.** Although not yet widely appreciated, the contribution of aggregative processes to particle and nanoparticle growth has been recognized at least since the work of Matijević,[17−19] Turkevich,[31] and Zukoski.[14,28,42,46,82] Aggregation is also an intrinsic component of growth by oriented attachment.[15,30,83,84] Theoretical studies by Zukoski and co-workers show small nanocrystals to be unstable with respect to aggregation on time scales shorter than those for classical growth.[28] Finke and co-workers have developed kinetics models that incorporate aggregative steps into nanoparticle-growth mechanisms.[13,22−25] More recently, Alivisatos and co-workers have directly observed nanoparticle aggregation and coalescence in the TEM.[6] Evidence for aggregative growth includes the observation of particles composed of smaller primary nanocrystals,[15,18,21,31,32,83−85] and decreasing particle number densities with time.[24,26−28] Indeed, decreasing particle number densities have been found in the growth of LaMer sulfur sols, arguing for the participation of aggregative processes even in this classic case.[86−88]

(80) Ben-Eliyahu, Y.; Brill, M.; Mintz, M. H. *J. Chem. Phys.* **1999**, *111*, 6053–6060.
(81) Wette, P.; Schöpe, H. J.; Palberg, T. *J. Chem. Phys.* **2005**, *123*, 174902.
(82) Look, J.-L.; Bogush, G. H.; Zukoski, C. F. *Faraday Discuss. Chem. Soc.* **1990**, *90*, 345–357.
(83) Penn, R. L. *J. Phys. Chem. B* **2004**, *108*, 12707–12712.
(84) Penn, R. L.; Banfield, J. F. *Geochim. Cosmochim. Acta* **1999**, *63*, 1549–1557.
(85) Matijević, E. *Chem. Mater.* **1993**, *5*, 412–426.
(86) Levit, A. B.; Rowell, R. L. *J. Colloid Interface Sci.* **1975**, *50*, 162–169.

Two recent studies are particularly relevant to the results presented here. Kraehnert, Emmerling, and co-workers studied the nucleation and growth of Au nanoparticles by reduction of tetrachloroauric acid, with monitoring by small-angle X-ray scattering and X-ray absorption near-edge spectroscopy.[44,45] The results provide strong evidence for the participation of aggregative processes. When the comparatively mild reducing agent citrate is employed, the time regimes for the chemical reduction, classical nucleation and growth, and aggregative growth overlap significantly.[44] However, when the stronger reducing agent sodium borohydride is employed, the reduction and classical nucleation and growth, resulting in small, primary nanocrystals (of size ~1 nm), is rapid and subsequently followed by a separate aggregative-growth regime.[45] The latter case parallels the findings reported here for Ag nanoparticles.

An important study of Ag-nanoparticle formation was reported by Van Hyning, Klemperer, and Zukoski several years ago.[14] They monitored nanoparticle growth by the borohydride reduction of Ag ions in aqueous solution. Their results foreshadowed those obtained later by Kraehnert, Emmerling, and co-workers for the borohydride reduction of tetrachloroauric acid.[45] Van Hyning, Klemperer, and Zukoski found that the concentration of Ag ions dropped by 2 orders of magnitude within the first 5 s of reaction, producing primary Ag nanocrystals having dimensions of about 2.5 nm. Subsequently, Ag-nanoparticle growth occurred over the next 20−50 min by aggregative processes involving the primary nanocrystals. Our results mimic those of Van Hyning, Klemperer, and Zukoski, although we have formed Ag nanoparticles from a molecular precursor and by eq 2, and have used general conditions that are quite different than those they employed.[14]

We demonstrated here and previously[21] that aggregative growth may be nucleation driven, and that the nucleation function for this nonclassical process may be experimentally determined (see Figure 10). The nucleation function is the key to achieving control over final nanoparticle mean sizes and size distributions. We showed previously that the time width of the nucleation function is strongly correlated with the size distribution, and that the width of the function may be purposely varied by a salt additive.[21] Furthermore, the area under the nucleation function is the number of critical aggregates formed, which is equal to the number of growth-viable nanoparticles, and thus the final number of nanoparticles. We showed previously that this area is strongly correlated with the final nanoparticle mean size.[21] Thus, important synthetic advances will be realized when the height and width of the aggregative-nucleation function can be systematically controlled.

## Conclusion

The results reported here establish that the pathway for the growth of Ag nanoparticles from $[(PPh_3)_2Ag(O_2CC_{13}H_{27})]$ according to eq 2 consists of four processes: precursor decomposition, classical or LaMer nucleation and growth, aggregative nucleation and growth, and Ostwald ripening. The three nanoparticle growth and ripening processes occur in consecutive time regimes. Precursor decomposition and classical nucleation and growth occur concurrently in the first regime. Although nanoparticles prepared from molecular precursors are generally considered to have grown by the LaMer mechanism, and nanoparticles prepared from smaller nanocrystals to have grown by Ostwald ripening, the results here and elsewhere[13,14,21−25,44,45] establish that aggregative growth can contribute prominently in both cases. Indeed, Ag-nanoparticle growth according to eq 2 is dominated by aggregative processes. Therefore, aggregative growth should be considered a potential contributing mechanism in all nanoparticle-forming reactions.

**Acknowledgment.** We thank Prof. Richard A. Loomis (Washington University) and Mr. Patricio La Rosa (Washington University) for helpful discussions. We thank Drs. Jeff Kao and Fudong Wang for technical assistance. We are grateful to the National Science Foundation for funding this work under Grant CHE-0518427, and for the purchase of the X-ray diffractometer under CHE-0420497.

**Supporting Information Available:** Tables of atomic coordinates, isotropic displacement parameters, bond lengths and angles, anisotropic displacement parameters, and torsion angles for $[(PPh_3)_2Ag(O_2CC_{13}H_{27})]$; energy-dispersive X-ray spectrum of Ag nanoparticles, ESI-MS, and $^{13}C\{1H\}$ NMR of the byproducts of eq 2; and a calibration plot of TEM Ag-nanoparticle mean diameter vs surface-plasmon absorbance (PDF). This material is available free of charge via the Internet at http://pubs.acs.org.

(87) Kerker, M.; Daby, E.; Cohen, G. L.; Kratohvil, J. P.; Matijević, E. *J. Phys. Chem.* **1963**, *67*, 2105–2111.
(88) Rowell, R. L.; Kratohvil, J. P.; Kerker, M. *J. Colloid Interface Sci.* **1968**, *27*, 501–506.